Rapid Communications

Topological phonons in graphene

Jiangxu Li,[1,2] Lei Wang,[1,2] Jiaxi Liu,[1,2] Ronghan Li,[1] Zhenyu Zhang,[3] and Xing-Qiu Chen[1,*]

[1]*Shenyang National Laboratory for Materials Science, Institute of Metal Research, Chinese Academy of Sciences, Shenyang 110016, China*

[2]*School of Materials Science and Engineering, University of Science and Technology of China, Shenyang 110016, Liaoning, China*

[3]*International Center for Quantum Design of Functional Materials (ICQD), Hefei National Laboratory for Physical Sciences at the Microscale, and Synergetic Innovation Center of Quantum Information and Quantum Physics, University of Science and Technology of China, Hefei 110016, China*

(Received 9 July 2019; revised manuscript received 15 January 2020; accepted 21 January 2020; published 12 February 2020)

By means of first-principles calculations and a modeling analysis, we have predicted that traditional two-dimensional graphene hosts four types of topological phononic Dirac points (DPs) and a phononic nodal ring (PNR) in its phonon spectrum. In the phonon spectrum of graphene, there exist four types of DPs, DP1, DP2, DP3, and DP4, with both DP1 and DP2 located at the Brillouin zone (BZ) corners K and K', DP3 located along the Γ-K line, and DP4 located along the Γ-M line, as well as the PNR surrounding the centered Γ point in the $q_{x,y}$ plane. The calculations further reveal that Berry curvatures are vanishingly zero throughout the whole BZ, except for the positions of these four Dirac phonons, at which the nonzero singular Berry curvatures appear with a Berry phase of π or $-\pi$, confirming its topological nontrivial nature. The topologically protected nontrivial phononic edge states have been also evidenced along both the zigzag-edged and armchair-edged boundaries. These results may pave the way for further studies of the topological phononic properties of graphene, such as phononic destructive interference with a suppression of backscattering and intrinsic phononic quantum Hall-like effects.

DOI: 10.1103/PhysRevB.101.081403

Graphene, consisting of one-atom-thick carbon in a two-dimensional (2D) hexagonal lattice, distinguishes itself as an ideal platform for various interesting and unusual properties, such as large, tunable carrier densities $n \sim 10^{11}$–10^{14} cm^{-2}, an ultrasmall, tunable Drude mass, exceptionally long intrinsic relaxation times, and so on. These are mainly because its electronic structure can be described at low energies by a massless Dirac-fermion model. On the basis of graphene, Kane and Mele contributed a pioneering theoretical discovery to predict its quantum spin Hall effect by breaking the Dirac cone into a gap by forcing a spin-orbit coupling interaction [1], witnessing a new phase of quantum matter, called topological insulators in HgTe [2,3], with insulating bulk and quantized and robust edge conductance. In parallel with electrons, still on the basis of the structure of graphene, the topological nature of the phonon Hall effect was theoretically proposed by interplaying Raman-type spin-phonon interactions [4], and infrared topological plasmons were also recently proposed by breaking time-reversal symmetry under a static magnetic field [5]. The other two time-reversal symmetry-breaking two-dimensional systems were theoretically proposed to show topological phonon states with robust one-way elastic edge waves [6,7], which are immune to backscattering. Interesting, in all these studies [1,4–7], time-reversal symmetry-breaking fields by gyroscopic inertial effects [6,7], spin-orbit coupling effects [1], spin-phonon interactions [4], and static magnetic fields [5] are necessary to induce topologically protected one-way electronic or phononic edge states on 2D systems. As early as 2008, phononic band crossing points were revealed in graphene [8]. Subsequently, chiral phonons at both the K and K' points in a two-dimensional hexagonal lattice including graphene have been discussed [9–12] and then such chiral phonons were called Dirac phonons [9–12]. In addition, Dirac phonons at the K and K' points and their corresponding boundary states have also been studied in detail for the monolayer hexagonal CrI_3 [13]. Yet, it is still not clear whether the other phonon modes of graphene are topological.

In Ref. [7], a modeling analysis for four phonon bands with the occurrence of a complete band gap for a hexagonal phononic crystal reveals that this gap is topologically trivial, since the time-reversal symmetry is not broken and the Chern numbers of the bands are all zero. It was the reason why the authors introduced gyroscopic coupling to their modeling to obtain the nontrivial topological nature. In similarity to this work, in Ref. [9] various novel topological effects of phonons, including topologically protected pseudospin-polarized interface states and the phonon pseudospin Hall effect, have been theoretically modeled in a Kekulé lattice. Returning to graphene, its unit cell has two carbon atoms allowing six degrees of freedom for atomic displacements. Even with equal masses for two carbon atoms, it is possible to have intrinsically topologically protected phononic states in graphene because of the two extra freedoms—vibration modes—along the direction normal to the xy plane, which definitely increase its perturbations. With such a purpose, we have revisited the issue of phonon dispersions of graphene. Interestingly, we have found that the topology is an intrinsic property of the phonon spectrum for graphene. Our calculations reveal that, in the 2D hexagonal Brillouin zone (BZ), Dirac phonons

*xingqiu.chen@imr.ac.cn

not only exist at two inequivalent K and K' points but also appear on the Γ-L and Γ-K lines. Four types of Dirac phonons are revealed in its BZ. More interesting, there still exists a phononic nodal ring (PNR) surrounding the centered Γ point. Furthermore, we have evidenced nontrivial edge states along both zigzag-edged and armchair-edged boundaries, which are indeed confined to the boundaries in one-way propagation.

Based on the density functional theory (DFT) [14,15] and density functional perturbation theory (DFPT) [16], we have calculated stable lattice constants and the phonon dispersion. Both DFT and DFPT calculations have been performed by the Vienna *ab initio* simulation package (VASP) [17–19]. We adopted the projector augmented-wave (PAW) [20,21] potentials and the generalized gradient approximation (GGA) within the Perdew-Burke-Ernzerhof (PBE) exchange-correlation function [22]. They treat semicore valence electrons as valence electrons. To obtain stable phonon spectra, a highly accurate optimization of the lattice constants has been performed by minimizing the interionic forces to within 0.0001 eV/Å. The cutoff energy for the expansion of the wave function into the plane waves was 550 eV. A Monkhorst-Pack k mesh ($21 \times 21 \times 1$) was used for the BZ integrations with a resolution of $2\pi \times 0.01$ Å. By trying various supercells for the calculations of phonon dispersions, it has been found that the $7 \times 7 \times 1$ supercell yielded a high accuracy to provide the most reliable force constants by combining both the VASP and PHONOPY codes [23]. Of course, we have also computed the phonon spectrum by including the spin-orbital coupling (SOC) effect, and the SOC does not exhibit any influence on the phonon. By using the force constants as hopping parameters, we have built dynamic matrices to analyze the topological nature. The boundary phonon dispersions have been performed by constructing a chain model, and the boundary-edged phonon densities of states have also been obtained by using the iteration Green's function method [24].

We have recalculated the phonon dispersions of graphene in Fig. 1, which is in good agreement with previous calculations [25–27]. Importantly, we have observed several linear crossings of the phonon bands in Fig. 1. At the K point, the BZ's corners, there are two linear crossings of the phonon bands, clearly stemming from the band crossing between the ZA and ZO branches at 15.92 THz and from another band crossing between the LA and LO branches at about 36.36 THz. The former is marked with DP1 and the latter with DP2 in Fig. 1. In addition, we still note that there exist two types of band crossings between the LO and TO branches along the Γ-M and Γ-K (or Γ-K') paths, defined as DP3 and DP4, respectively. In particular, these four crossing points (DP1, DP2, DP3, and DP4) are isolated points, showing a conical band structure on the $q_{x,y}$ plane. The DP1 has the lowest frequency among those four crossings. We have plotted the band structure between the ZA and ZO branches on the $q_{x,y}$ plane of the BZ in Figs. 2(a) and 2(b) from which the conical structure can be clearly evidenced. Interestingly, the conical shapes of DP2 and DP3 are very similar to that of DP1, although their frequencies are different. However, the conical shape of DP4 is highly different, as its conical structure on the $q_{x,y}$ plane is tilted as shown in Fig. 2(c). To identify whether these four DPs exhibit a topological nature, we have calculated their Berry curvatures on a 2D $q_{x,y}$ plane. It needs

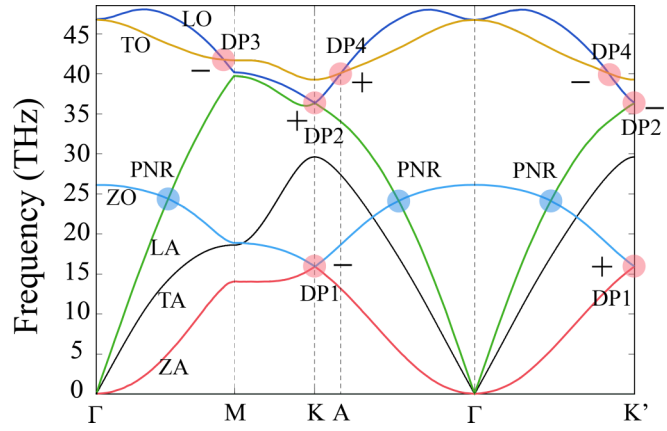

FIG. 1. The DFT-PBE derived phonon dispersions of graphene. ZA: Out-of-plane acoustic branch. ZO: Out-of-plane optical branch. TA: Transverse-acoustic branch. TO: Transverse-optical branch. LA: Longitudinal-acoustic branch. LO: Longitudinal-optical branch. Note that the seven phononic Dirac nodes are marked by pink transparent circles, and the three blue circles are three nodal points on the nodal line formed by the crossing between the lowest out-of-plane optical (ZO) and the highest longitudinal-acoustic (LA) branches. The Berry phases of these Dirac nodes are marked as "+" for π and "−" for $-\pi$.

to be emphasized that for 2D crystals the Berry curvature only has a nonzero value (Ω_{xy}) along the q_z direction, whereas Ω_{yz} and Ω_{zx} have to be zero. Here, we have selected DP1 and DP4 as the examples. Figures 2(d) and 2(e) show the Berry curvatures of the ZA/ZO crossing (DP1) at K and K', indicating that their Berry curvatures only have an extremum exactly at K and K' but with opposite signs, and at all other positions the Berry curvature is strictly zero. This reveals that the DP1 at K and K' have opposite charges. Furthermore, both DP2 and DP3 show a similar feature to DP1. We have also calculated the Berry curvature of DP4 on the 2D $q_{x,y}$ plane in Fig. 2(f), evidencing the isolated maximum value only at the defined A point along the Γ-K path, whereas the Berry curvature at any other q point is almost zero. Moreover, we have calculated their Berry phases as

$$\gamma_n = \oint_C \mathbf{A}_n(\mathbf{q}) \cdot d\mathbf{l}, \tag{1}$$

where $\mathbf{A}_n(\mathbf{q}) = i\langle u_n(\mathbf{q})|\nabla_q|u_n(\mathbf{q})\rangle$ is the Berry connection and $u_n(\mathbf{q})$ is the Bloch wave function of the nth band. For this purpose, we have defined a circle on the $q_{x,y}$ plane centered at the $q = K$ momentum to calculate the Berry phase. The radius of the circle going around this K point can be selected to be arbitrarily large, as long as it does not also cover another K or K' point. Interestingly, the Berry phase for this crossing point DP1 at K is $-\pi$, whereas another crossing point at K' has an opposite Berry phase of π. This means that the two crossing points of DP1 at K or K' are topologically nontrivial and it also proves that the topological properties of the band crossings at K or K' are opposite in their Berry phase. Therefore, these band crossing points, DP1, at K and K' are indeed a pair of Dirac nodes with an opposite Berry phase. Thus, we have also analyzed the Berry phases of the other three crossing points (DP2, DP3, and DP4), revealing

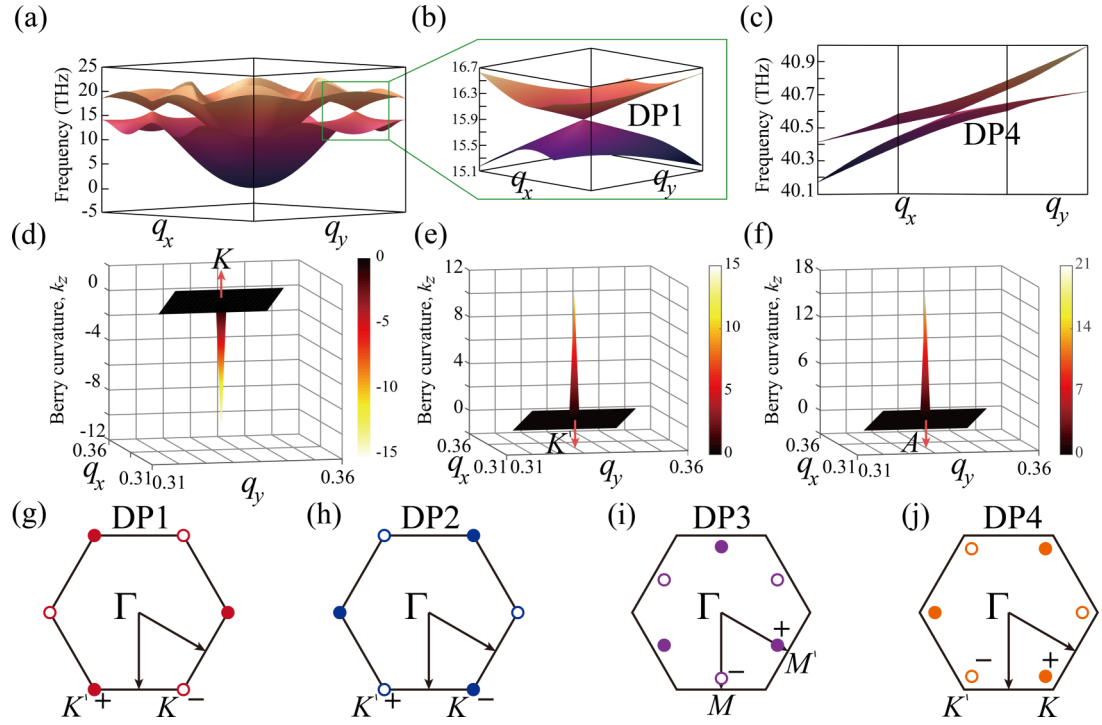

FIG. 2. Dirac phonons at K and K' in graphene. (a) The 3D visualization of the DFT-PBE derived phonon ZA and ZO branches of graphene to show the linear crossing, PW1, at the K and K' point in the BZ. (b) Zoom-in 3D visualization of both ZA and ZO branches surrounding the K point of the BZ. (c) Visualized DFT-PBE derived phonon LO and TO branches of graphene to show the linear crossing, PW4, along the Γ and K path in the BZ. (d) and (e) Derived Berry curvature surrounding the phononic Dirac point, DP1, at K (or K') point on the $q_{x,y}$ plane ($q_x = 0.31$–0.36; $q_y = 0.31$–0.36) of the BZ. (f) Distribution of Berry curvature of the Dirac point, DP4, at the defined A point of the 2D BZ. (g)–(j) Distribution of the Dirac points in the first BZ of graphene, DP1, DP2, DP3, and DP4, respectively.

that they have the same topological property as DP1 with a value of π or $-\pi$. Therefore, all four crossing points of DP1, DP2, DP3, and DP4 are 2D phononic Dirac points. It needs to be emphasized that all these 2D phononic Dirac points in graphene are intrinsically different from Weyl fermions [28–60] or phonons [61–67], although both of them are twofold degenerate. Because the lattice of graphene is such a system with both inversion and time-reversal symmetries, the phononic band crossing points do not possess the characteristics of Weyl nodes. Of course, 3D shapes for these DPs are physically not allowed for graphene. In addition, DP1, DP2, and DP3 exhibit a normal conical shape, whereas the DP4 has a tilted conical shape. All these Dirac nodes obey threefold rotation symmetry and thus each type of Dirac point has three pairs in its 2D first BZ, as illustrated in Figs. 2(g)–2(j).

We have still noted that at 24 THz the phononic linear band crossings occur between the LA and ZO branches along the Γ-K (or K') and Γ-M directions (Fig. 1). Importantly, these three linear crossing points are not isolated and, instead, they form a closed PNR around the Γ point in the BZ. In order to clearly see the shape of the PNR, we have visualized the phonon bands of both ZO and LA branches on the $q_{x,y}$ plane in Fig. 3(a). The specified location of the PNR is shown in the BZ in Fig. 3(b) in which we have used the gap between the ZO and LA branches to obtain the PNR distribution, evidencing the occurrence of the black circle centered at the Γ point.

For a 2D crystal, the topologically nontrivial nature can be observed by the edge states. To elucidate this feature, we have employed the phononic tight-binding model to construct the supercell of a ribbon model [Fig. 3(a)] along different directions, and the edge phononic bands are obtained by a truncated chain of graphene. Through the Green's function iteration method, the 2D and edge phononic densities of states can be obtained through the imaginary parts of the Green's function. Currently, we have mainly focused on the two representative edge states of the zigzag-edged boundary [the [100] direction in Fig. 4(a)] and of the armchair-edged boundary (the $[1\bar{1}0]$ direction) as shown in the Supplemental Material [68]. From the phonon dispersions of the zigzag-edged boundary in Fig. 4(b), four distinct topologically protected nontrivial edge phononic states can be observed. In the first, at about 16 THz of the zigzag-edged phononic states, a straight-line state is formed to connect two projected DP1

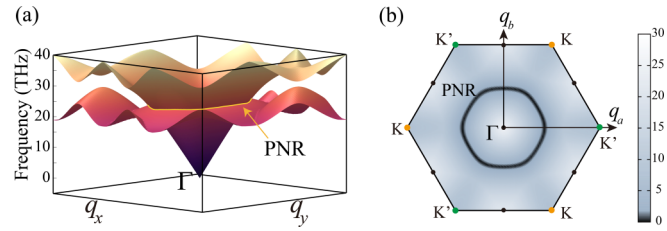

FIG. 3. (a) The 3D visualization of the DFT-PBE derived phonon ZO and LA branches of graphene to show the phononic nodal line surrounding the Γ point in the BZ. (b) The gap between these two ZO/LA branches in the first BZ. The black circle represents the PNR on $q_{x,y}$ plane.

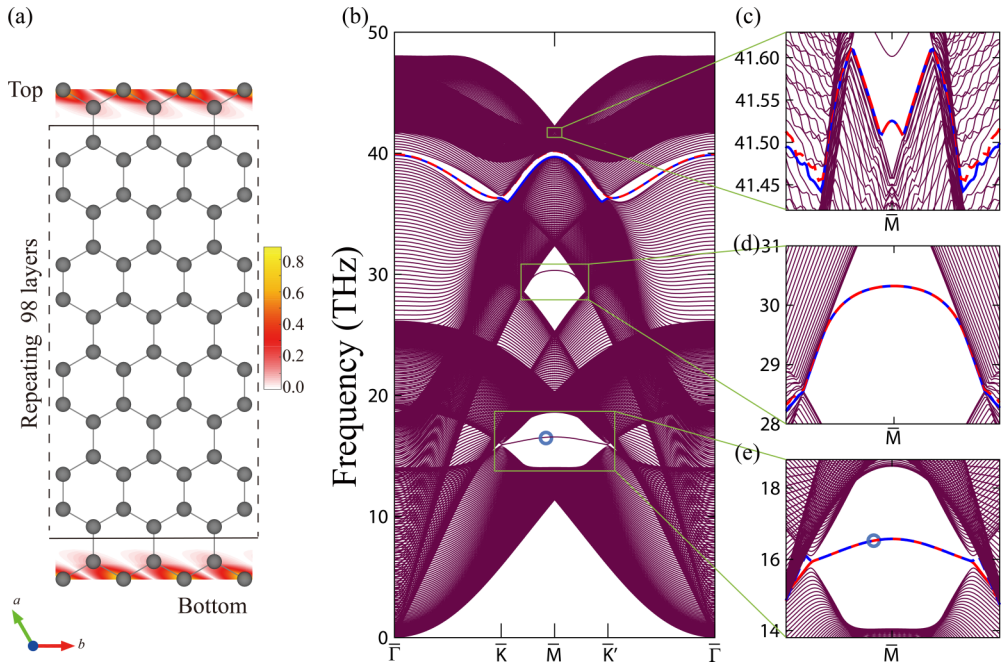

FIG. 4. The phonon dispersions of the zigzag-edged boundaries (along the [100] direction) of graphene. (a) The ribbon model of graphene with a zigzag-edged boundary. (b) The phonon dispersion of the ribbon model derived by the tight-binding calculations along the zigzag-edged high-symmetry paths. (c)–(e) Zoom-in local phonon dispersions connecting to the projection sites of the DP3, PNR, and DP1 phonons around the $\overline{M}$ point. Note that we have plotted the edge states in (a) on a selected point [as marked by a circle in (b)] of the DP1-induced topologically protected phononic edge dispersion.

points with opposite Berry phases. To illuminate the edge states, we have analyzed the Blöch modes of a selected point on the edge states. As shown in Figs. 4(b) and 4(e), the point is marked by a blue circle on the edge states and its coordinate is $q = (0.45, 0.0)\frac{2\pi}{a}$. This twofold degenerate band originates from the ZA and ZO modes of the pristine phonons of graphene. From the tight-binding model, we have analyzed the vibration modes of these two phononic bands on the edge states. As expected, these two edge bands are associated with the out-of-plane vibration modes only along the k_z direction for the edged carbon atoms in Fig. 4(a), which are exactly the same as the ZA and ZO modes correlated with the DP1 Dirac nodes of pristine graphene. In particular, at $q = (0.5, 0.0)\frac{2\pi}{a}$, each of the twofold degenerate phonon edge bands is only contributed by the carbon atoms at the zigzag boundaries. As illustrated in Fig. 4(a), the sharp spatial Blöch modes of those two phononic bands are strictly confined at the zigzag edges. This means that the twofold degenerate edged states only propagate along the edged boundaries. Remarkably, this straight-line phononic edge state has a nearly flat phononic dispersion upon various q momenta from $\overline{K}$ to $\overline{K'}$, as illustrated in Fig. 4(e). It reveals that the phononic edge states originating from the DP1 Dirac points have nearly zero phonon group velocity [namely, $v(q) \approx 0$] in the phonon one-way transport direction along the zigzag-edged boundary of graphene. This interesting feature of a zigzag-edged narrow ribbon of graphene may have potential applications for the emitting of ultraslow light. Of course, we have also analyzed other points of the phononic edge states, revealing similar spatial and local properties of the vibrations. In the second, for DP2 at 36.36 THz there is a distinct twofold edge state connecting two PW2-projected points with a different Berry phase as shown in Fig. 4(b), which is marked by red and blue lines. At around 41.50 THz, the other phonon edge states can be also visualized to connect the DP3 Dirac points with opposite Berry phase, as shown in Fig. 4(c). In comparison with the edge states induced by DP1 and DP2, the DP3-induced edge states are not only shorter in the q momentum but also exhibit relatively larger dispersions. Moreover, it needs to be emphasized that for DP4 no edge states can be clearly observed because the DP4-induced topologically protected phononic edge states fully overlap with the edge projection from the phonon dispersions of pristine graphene. In the third, in similarity to the nodal lines in 3D crystals which exhibit nontrivial drumheadlike surface states for pure alkali-earth metals (Be, Mg, Ca, and Sr) [69,70], and the compounds of $BaSn_2$, Ca_3P, $TlTaSe_2$, TiSi, and ZrSiS [71–75], as well as the phononic nodal line MgB_2 [63], the existence of PNR of pristine graphene at 24.38 THz induces straight-line edge states, simultaneously, with an arclike downwards parabola in its frequencies upon the q momentum, as shown in Fig. 4(d). Moreover, the topological phonon-induced edge states for an armchair-edged boundary of graphene are also further discussed in the Supplemental Material [68].

It needs to be emphasized that, in general, a nodal ring in a two-dimensional material, which hosts a nontrivial topological charge within its interior, would not exhibit any topological edge states, because the codimension of the projected nodal line of this nodal ring onto any edge boundary is zero [76,77]. In contrast, the PNR in graphene is different and it hosts topologically nontrivial drumheadlike edge states on the zigzag-edged boundaries. It is clear that the PNR in graphene is formed by an inverted phononic band between an optical branch (ZO) and an acoustic branch (LA) centering at the Γ

point and, hence, the topological charge of this PNR must be trivial within its interior by also including the centered Γ point. Because the frequency of the acoustic LA branch has to be zero at the Γ point, within the PNR's interior the normal phononic band ordering always exists. This reveals that outside this PNR the nontrivial topological charge certainly occurs. Otherwise, it is impossible to form the PNR between the ZO and LA branches. The details are analyzed in the Supplemental Material [68]. Because the phononic band inversion occurs outside the PNR, the general principle of the codimension [76,77] no longer fits the PNR case of graphene. Therefore, the PNR in graphene will certainly induce the topologically nontrivial edge states outside its projection line. This is what we have exactly observed, as shown by the derived edge states in Fig. 4(d), which are formed by the ZO and LA phonon modes on the edged boundary.

The occurrence of phononic Dirac nodes in the BZ is very important for graphene, which provides an ideal platform to study novel topological phononic properties, such as destructive interference and quantum (anomalous/spin) Hall-like topological effects. First, the chiral electrons in graphene [78] moving along a closed path have been demonstrated to exhibit a phase change of the two components of the wave function. This leads to a different phase, which contributes to the interference processes. In similarity to electrons in graphene, the Dirac phonons at both K and K' have opposite Berry phases for both DP1 and DP2. If a phonon traverses such a closed path without being scattered, protected by the DP-induced nontrivial phononic edge states, from a DP at K to the other DP at K', the Berry phase definitely changes its sign of the amplitude of one path with respect to the time-reversed path [78]. Therefore, these two paths possibly form so-called destructive interference, as accompanied with a suppression of backscattering. As shown in Fig. 4(a) for the robust phononic nontrivial edge states induced by DP1 along the K to K' path, phonon destructive interference would be reasonably expected. Similar behaviors would also hold for both DP3 in the $\bar{\Gamma}$-$\bar{M}$ direction and DP4 along the $\bar{\Gamma}$-$\bar{K}$ direction. Second, it is interesting to emphasize that, as shown in Fig. 2, the Berry curvatures are vanishingly zero throughout the BZ, except for the positions of the four types of DPs (Fig. 2). At these DPs, the nonzero Berry curvatures (corresponding to the Berry phase of π and $-\pi$) appear, associated with DP1, DP2, DP3, and DP4 (Fig. 2). They can be indeed viewed as a magnetic field in the momentum space, accordingly leading to the possible occurrence of phononic quantum (anomalous/spin) Hall-like topological effects.

Through first-principles calculations and a modeling analysis we have revealed the existence of intrinsic topological Dirac and PNR phonons in pristine graphene, as accompanied with the robust appearance of topologically protected one-way phononic edge states. Given the fact that many interesting physical properties are related with phonons, graphene would be an ideal case to elucidate the fundamental physical phenomena related to topological phonons, possibly including heat conduction, electrical resistance, and phonon waveguides, as well as electron-phonon coupling effects for superconductivity.

Work was supported by the National Science Fund for Distinguished Young Scholars (No. 51725103) and by the National Natural Science Foundation of China (Grant No. 51671193). All calculations have been performed on the high-performance computational cluster in the Shenyang National University Science and Technology Park.

[1] C. L. Kane and E. J. Mele, Quantum Spin Hall Effect in Graphene, Phys. Rev. Lett. **95**, 226801 (2005).
[2] B. A. Bernevig, T. L. Hughes, and S.-C. Zhang, Quantum spin Hall effect and topological phase transition in HgTe quantum wells, Science **314**, 1757 (2006).
[3] M. König, S. Wiedmann, C. Brüne, A. Roth, H. Buhmann, L. W. Molenkamp, X.-L. Qi, and S.-C. Zhang, Quantum spin Hall insulator state in HgTe quantum wells, Science **318**, 766 (2007).
[4] L. Zhang, J. Ren, J.-S. Wang, and B. Li, Topological Nature of the Phonon Hall Effect, Phys. Rev. Lett. **105**, 225901 (2010).
[5] D. Jin, T. Christensen, M. Soljacic, N. X. Fang, L. Lu, and X. Zhang, Infrared Topological Plasmons in Graphene, Phys. Rev. Lett. **118**, 245301 (2017).
[6] E. Prodan and C. Prodan, Topological Phonon Modes and Their Role in Dynamic Instability of Microtubules, Phys. Rev. Lett. **103**, 248101 (2009).
[7] P. Wang, L. Lu, and K. Bertoldi, Topological Phononic Crystals with One-Way Elastic Edge Waves, Phys. Rev. Lett. **115**, 104302 (2015).
[8] K. H. Michel and B. Verberck, Theory of the evolution of phonon spectra and elastic constants from graphene to graphite, Phys. Rev. B **78**, 085424 (2008).
[9] Y. Z. Liu, C.-S. Lian, Y. Li, Y. Xu, and W. H. Duan, Pseudospins and Topological Effects of Phonons in a Kekulé Lattice, Phys. Rev. Lett. **119**, 255901 (2017).
[10] L. F. Zhang and Q. Niu, Chiral Phonons at High-Symmetry Points in Monolayer Hexagonal Lattices, Phys. Rev. Lett. **115**, 115502 (2015).
[11] Y.-T. Wang, P.-G. Luan, and S. Zhang, Coriolis force induced topological order for classical mechanical vibrations, New J. Phys. **17**, 073031 (2015).
[12] T. Kariyado and Y. Hatsugai, Manipulation of Dirac cones in mechanical graphene, Sci. Rep. **5**, 18107 (2015).
[13] Y. J. Jin, R. Wang, and H. Xu, Recipe for Dirac phonon states with a quantized valley Berry phase in two-dimensional hexagonal lattices, Nano Lett. **18**, 7755 (2018).
[14] P. Hohenberg and W. Kohn, Inhomogeneous electron gas, Phys. Rev. **136**, B864 (1964).
[15] W. Kohn and L. J. Sham, Self-consistent equations including exchange and correlation effects, Phys. Rev. **140**, A1133 (1965).
[16] S. Baroni, S. D. Gironcoli, A. D. Corso, and P. Giannozzi, Phonons and related crystal properties from density-functional perturbation theory, Rev. Mod. Phys. **73**, 515 (2001).
[17] G. Kresse and J. Hafner, *Ab initio* molecular dynamics for liquid metals, Phys. Rev. B **47**, 558 (1993).

[18] G. Kresse and J. Hafner, *Ab initio* molecular-dynamics simulation of the liquid-metal amorphous-semiconductor transition in germanium, Phys. Rev. B **49**, 14251 (1994).
[19] G. Kresse and J. Furthmüller, Efficiency of *ab-initio* total energy calculations for metals and semiconductors using a plane-wave basis set, Comput. Mater. Sci. **6**, 15 (1996).
[20] P. E. Blöhl, Projector augmented-wave method, Phys. Rev. B **50**, 17953 (1994).
[21] G. Kresse and D. Joubert, From ultrasoft pseudopotentials to the projector augmented-wave method, Phys. Rev. B **59**, 1758 (1999).
[22] J. P. Perdew, K. Burke, and M. Ernzerhof, Generalized Gradient Approximation Made Simple, Phys. Rev. Lett. **77**, 3865 (1996).
[23] L. Chaput, A. Togo, I. Tanaka, and G. Hug, Phonon-phonon interactions in transition metals, Phys. Rev. B **84**, 094302 (2011).
[24] M. P. Sancho, J. M. Sancho, and J. Rubio, Highly convergent schemes for the calculation of bulk and surface Green functions, J. Phys. F: Met. Phys. **15**, 851 (1985).
[25] N. Mounet and N. Marzari, First-principles determination of the structural, vibrational and thermodynamic properties of diamond, graphite, and derivatives, Phys. Rev. B **71**, 205214 (2005).
[26] N. Bonini, M. Lazzeri, N. Marzari, and F. Mauri, Phonon Anharmonicities in Graphite and Graphene, Phys. Rev. Lett. **99**, 176802 (2007).
[27] D. L. Nika, E. P. Pokatilov, A. S. Askerov, and A. A. Balandin, Phonon thermal conduction in graphene: Role of Umklapp and edge roughness scattering, Phys. Rev. B **79**, 155413 (2009).
[28] H. Weyl, Elektron und Gravitation. I, Z. Phys. **56**, 330 (1929).
[29] X. Wan, A. M. Turner, A. Vishwanath, and S. Y. Savrasov, Topological semimetal and Fermi-arc surface states in the electronic structure of pyrochlore iridates, Phys. Rev. B **83**, 205101 (2011).
[30] S.-M. Huang, X.-Y. Xu, I. Belopolski, C.-C. Lee, G. Q. Chang, B. K. Wang, N. Alidoust, G. Bian, M. Neupane, C. L. Zhang, S. Jia, A. Bansil, H. Lin, and M. Z. Hasan, A Weyl Fermion semimetal with surface Fermi arcs in the transition metal monopnictide TaAs class, Nat. Commun. **6**, 7373 (2015).
[31] H. M. Weng, C. Fang, Z. Fang, B. A. Bernevig, and X. Dai, Weyl Semimetal Phase in Noncentrosymmetric Transition-Metal Monophosphides, Phys. Rev. X **5**, 011029 (2015).
[32] S.-Y. Xu *et al.*, Discovery of a Weyl fermion state with Fermi arcs in niobium arsenide, Nat. Phys. **11**, 748 (2015)
[33] S.-Y. Xu *et al.*, Discovery of a Weyl fermion semimetal and topological Fermi arcs, Science **349**, 613 (2015).
[34] A. A. Soluyanov, D. Gresch, Z. Wang, Q. S. Wu, M. Troyer, X. Dai, and B. A. Bernevig, Type-II Weyl semimetals, Nature (London) **527**, 495 (2015).
[35] Y. Sun, S.-C. Wu, M. N. Ali, C. Felser, and B. H. Yan, Prediction of Weyl semimetal in orthorhombic $MoTe_2$, Phys. Rev. B **92**, 161107(R) (2015).
[36] R. Yu, Q. S. Wu, Z. Fang, and H. M. Weng, From Nodal Chain Semimetal to Weyl Semimetal in HfC, Phys. Rev. Lett. **119**, 036401 (2017).
[37] C. Fang, M. J. Gilbert, X. Dai, and B. A. Bernevig, Multi-Weyl Topological Semimetals Stabilized by Point Group Symmetry, Phys. Rev. Lett. **108**, 266802 (2012).
[38] T. Dubček, C. J. Kennedy, L. Lu, W. Ketterle, M. Soljačič, and H. Buljan, Weyl Points in Three-Dimensional Optical Lattices: Synthetic Magnetic Monopoles in Momentum Space, Phys. Rev. Lett. **114**, 225301 (2015).
[39] L. Lu, J. D. Joannopoulos, and M. Soljačič, Topological photonics, Nat. Photonics **8**, 821 (2014).
[40] L. Lu, L. Fu, J. D. Joannopoulos, and M. Soljačič, Weyl points and line nodes in gyroid photonic crystals, Nat. Photonics **7**, 294 (2013).
[41] Q. Lin, M. Xiao, L. Yuan, and S. Fan, Photonic Weyl point in a two-dimensional resonator lattice with a synthetic frequency dimension, Nat. Commun. **7**, 13731 (2016).
[42] W.-J. Chen, M. Xiao, and C. T. Chan, Photonic crystals possessing multiple Weyl points and the experimental observation of robust surface states, Nat. Commun. **7**, 13038 (2016).
[43] J. Noh, S. Huang, D. Leykam, Y. D. Chong, K. P. Chen, and M. C. Rechtsman, Experimental observation of optical Weyl points and Fermi arc-like surface states, Nat. Phys. **13**, 611 (2017).
[44] H. He, C. Qiu, L. Ye, X. Cai, X. Fan, M. Ke, F. Zhang, and Z. Liu, Topological negative refraction of surface acoustic waves in a Weyl phononic crystal, Nature (London) **560**, 61 (2018).
[45] M. Xiao, W.-J. Chen, W.-Y. He, and C. T. Chan, Synthetic gauge flux and Weyl points in acoustic systems, Nat. Phys. **11**, 920 (2015).
[46] Z. Yang, F. Gao, X. Shi, X. Lin, Z. Gao, Y. Chong, and B. Zhang, Topological Acoustics, Phys. Rev. Lett. **114**, 114301 (2015).
[47] I. Belopolski *et al.*, Criteria for Directly Detecting Topological Fermi Arcs in Weyl Semimetals, Phys. Rev. Lett. **116**, 066802 (2016).
[48] J. Ahn and B.-J. Yang, Unconventional Topological Phase Transition in Two-Dimensional Systems with Space-Time Inversion Symmetry, Phys. Rev. Lett. **118**, 156401 (2017).
[49] Y. Xu, F. Zhang, and C. Zhang, Structured Weyl Points in Spin-Orbit Coupled Fermionic Superfluids, Phys. Rev. Lett. **115**, 265304 (2015).
[50] D. Z. Rocklin, B. G. Chen, M. Falk, V. Vitelli, and T. C. Lubensky, Mechanical Weyl Modes in Topological Maxwell Lattices, Phys. Rev. Lett. **116**, 135503 (2016).
[51] Z. Yan and Z. Wang, Tunable Weyl Points in Periodically Driven Nodal Line Semimetals, Phys. Rev. Lett. **117**, 087402 (2016).
[52] J. Ruan, S.-K. Jian, H. Yao, H. Zhang, S.-C. Zhang, and D. Xing, Symmetry-protected ideal Weyl semimetal in HgTe-class materials, Nat. Commun. **7**, 11136 (2016).
[53] Z. Gao, M. Hua, H. Zhang, and X. Zhang, Classification of stable Dirac and Weyl semimetals with reflection and rotational symmetry, Phys. Rev. B **93**, 205109 (2016).
[54] L. Lu, Z. Wang, D. Ye, L. Ran, L. Fu, J. D. Joannopoulos, and M. Soljačič, Experimental observation of Weyl points, Science **349**, 622 (2015).
[55] B. Q. Lv, Z.-L. Feng, Q.-N. Xu, X. Gao, J.-Z. Ma, L.-Y. Kong, P. Richard, Y.-B. Huang, V. N. Strocov, C. Fang, H.-M. Weng, Y.-G. Shi, T. Qian, and H. Ding, Observation of three-component fermions in the topological semimetal molybdenum phosphide, Nature (London) **546**, 627 (2017).
[56] J. Gooth, A. C. Niemann, T. Meng, A. G. Grushin, K. Landsteiner, B. Gotsmann, F. Menges, M. Schmidt, C. Shekhar, V. Süß, R. Hühne, B. Rellinghaus, C. Felser, B. Yan, and K. Nielsch, Experimental signatures of the mixed

axial-gravitational anomaly in the Weyl semimetal NbP, Nature (London) **547**, 324 (2017).

[57] H. Inoue, A. Gyenis, Z. Wang, J. Li, S. Woo Oh, S. Jiang, N. Ni, B. A. Bernevig, and A. Yazdani, Quasiparticle interference of the Fermi arcs and surface-bulk connectivity of a Weyl semimetal, Science **351**, 1184 (2016).

[58] H. M. Weng, C. Fang, Z. Fang, and X. Dai, Coexistence of Weyl fermion and massless triply degenerate nodal points, Phys. Rev. B **94**, 165201 (2016).

[59] H. M. Weng, C. Fang, Z. Fang, and X. Dai, Topological semimetals with triply degenerate nodal points in θ-phase tantalum nitride, Phys. Rev. B **93**, 241202(R) (2016).

[60] S. Wang, B.-C. Lin, A.-Q. Wang, D.-P. Yu, and Z.-M. Liao, Quantum transport in Dirac and Weyl semimetals: A review, Adv. Phys.: X **2**, 518 (2017).

[61] J. X. Li, Q. Xie, S. Ullah, R. H. Li, H. Ma, D. Z. Li, Y. Y. Li, and X.-Q. Chen, Coexistent three-component and two-component Weyl phonons in TiS, ZrSe, and HfTe, Phys. Rev B **97**, 054305 (2018).

[62] Q. Xie, J. X. Li, S. Ullah, R. H. Li, L. Wang, D. Z. Li, Y. Y. Li, S. Yunoki, and X.-Q. Chen, Phononic Weyl points and one-way topologically protected nontrivial phononic surface arc states in noncentrosymmetric WC-type materials, Phys. Rev. B **99**, 174306 (2019).

[63] J. X. Li, Q. Xie, J. X. Liu, R. H. Li, M. Liu, L. Wang, D. Z. Li, Y. Y. Li, and X.-Q. Chen, Phononic Weyl nodal straight lines in MgB_2, Phys. Rev. B **101**, 024301 (2020).

[64] O. Stenull, C. L. Kane, and T. C. Lubensky, Topological Phonons and Weyl Lines in Three Dimensions, Phys. Rev. Lett. **117**, 068001 (2016).

[65] T. T. Zhang, Z. D. Song, A. Alexandradinata, H. M. Weng, C. Fang, L. Lu, and Z. Fang, Double-Weyl Phonons in Transition-Metal Monosilicides, Phys. Rev. Lett. **120**, 016401 (2018).

[66] H. Miao, T. T. Zhang, L. Wang, D. Meyers, A. H. Said, Y. L. Wang, Y. G. Shi, H. M. Weng, Z. Fang, and M. P. M. Dean, Observation of Double Weyl Phonons in Parity-Breaking FeSi, Phys. Rev. Lett. **121**, 035302 (2018).

[67] S. Singh, Q. S. Wu, C. M. Yue, A. H. Romero, and A. A. Soluyanov, Topological phonons and thermoelectricity in triple-point metals, Phys. Rev. Mater. **2**, 114204 (2018).

[68] See Supplemental Material at http://link.aps.org/supplemental/10.1103/PhysRevB.101.081403 for discussions of the topologically protected nontrivial phononic edge states of the armchair-edged boundaries of graphene.

[69] R. H. Li, H. Ma, X. Y. Cheng, S. L. Wang, D. Z. Li, Z. Y. Zhang, Y. Y. Li, and X.-Q. Chen, Dirac Node Lines in Pure Alkali Earth Metals, Phys. Rev. Lett. **117**, 096401 (2016).

[70] R. H. Li, J. X. Li, L. Wang, J. X. Liu, H. Ma, H.-F. Song, D. Z. Li, Y. Y. Li, and X.-Q. Chen, Underlying Topological Dirac Nodal Line Mechanism of the Anomalously Large Electron-Phonon Coupling Strength on a Be (0001) Surface, Phys. Rev. Lett. **123**, 136802 (2019).

[71] H. Huang, J. P. Liu, D. Vanderbilt, and W. H. Duan, Topological nodal-line semimetals in alkaline-earth stannides, germanides, and silicides, Phys. Rev. B **93**, 201114 (2016).

[72] M. Neupane, I. Belopolski, M. M. Hosen, D. S. Sanchez, R. Sankar, M. Szlawska, S.-Y. Xu, K. Dimitri, N. Dhakal, P. Maldonado, P. M. Oppeneer, D. Kaczorowski, F. Chou, M. Z. Hasan, and T. Durakiewicz, Observation of topological nodal fermion semimetal phase in ZrSiS, Phys. Rev. B **93**, 201104(R) (2016).

[73] J. X. Li, H. Ma, Q. Xie, S. B. Feng, S. Ullah, R. Li, J. Dong, D. Z. Li, Y. Y. Li, and X.-Q. Chen, Topological quantum catalyst: Dirac nodal line states and a potential catalyst of hydrogen evolution in the TiSi-family, Sci. China Mater. **61**, 23 (2018).

[74] Y.-H. Chan, C.-K. Chiu, M. Y. Chou, and A. P. Schnyder, Ca_3P_2 and other topological semimetals with line nodes and drumhead surface states, Phys. Rev. B **93**, 205132 (2016).

[75] G. Bian, T.-R. Chang, H. Zheng, S. Velury, S.-Y. Xu, T. Neupert, C.-K. Chiu, S.-M. Huang, D. S. Sanchez, I. Belopolski, N. Alidoust, P.-J. Chen, G. Chang, A. Bansil, H.-T. Jeng, H. Lin, and M. Z. Hasan, Drumhead surface states and topological nodal-line fermions in $TlTaSe_2$, Phys. Rev. B **93**, 121113 (2016).

[76] C. K. Chiu and A. P. Schnyder, Classification of reflection-symmetry-protected topological semimetals and nodal superconductors, Phys. Rev. B **90**, 205136 (2014).

[77] Y. X. Zhao and Z. D. Wang, Topological Classification and Stability of Fermi Surfaces, Phys. Rev. Lett. **110**, 240404 (2013).

[78] A. H. Castro Neto, F. Guinea, N. M. R. Peres, K. S. Novoselov, and A. K. Geim, The electronic properties of graphene, Rev. Mod. Phys. **81**, 109 (2009).